Applied Science, Computing and Energy, 2026, 4(4), 570-581

Thickness-Controlled Transport–Reaction Regime Transition in Perovskite Solar Cells: A SCAPS-1D Dimensionless Flux–Kinetics Framework

Ejikeme Ezo Igbokwe, and Ho Soonmin
Received: 22 March 2026/Accepted: 26 June 2026/Published: 20 June May 2026

Abstract: *The integration of photovoltaic devices with surface-driven chemical processes offers a promising pathway for sustainable energy conversion. However, conventional modeling approaches typically treat charge transport and reaction kinetics independently, limiting the identification of performance bottlenecks in coupled systems. In this work, a transport–reaction framework is developed to directly link photovoltaic charge transport with surface reaction kinetics. A SnO_2/$CsPbI_2Br$/CuI perovskite solar cell is simulated using SCAPS-1D, and the electron flux (Φ_e) is extracted from the maximum power point current density. A dimensionless coupling parameter, $\Phi = \Phi_e/k$, is introduced to quantify the balance between charge supply and reaction demand. The results reveal a transition from reaction-limited ($\Phi \gg 1$) to transport-limited ($\Phi \ll 1$) regimes at $\Phi = 1$. The electron flux imposes an upper bound on sustainable reaction rates, with a critical transition occurring at $k \approx 10^{16}$–10^{17} s^{-1}. This behavior is analogous to a Damköhler-type scaling, highlighting the competition between transport and reaction processes. The proposed framework provides a generalizable framework for optimizing coupled photovoltaic–reaction systems.*

Keywords: *perovskite solar cells; SCAPS-1D; charge transport; reaction kinetics; hybrid energy systems; dimensionless analysis; transport–reaction coupling*

Ejikeme Ezo Igbokwe
Department of Physics with Electronics, Ogbonnaya Onu Polytechnic, Aba, Nigeria
Email: ejikeme.igbokwe@abiastatepolytechnic.edu.ng
https://orcid.org/0000-0003-1834-8614

Ho Soonmin
Faculty of Health and Life Sciences, INTI International University, Malaysia
Email: soonmin.ho@newinti.edu.my
https://orcid.org/0000-0002-3697-5091

1.0 Introduction The integration of photovoltaic (PV) devices with surface-driven chemical processes has emerged as a promising strategy for sustainable energy conversion, environmental remediation, and solar fuel production. By coupling light-harvesting materials with interfacial catalytic reactions, these systems can simultaneously generate electrical energy and drive chemical transformations, thereby enhancing solar energy utilization efficiency. (Fujishima & Honda, 1972). In such coupled systems, photogenerated charge carriers are not only extracted as electrical power but can also participate directly in interfacial reactions, including photocatalysis and solar fuel generation (Gong *et al*., 2019). Recent advances in perovskite-based photovoltaic technologies have further stimulated interest in integrating these materials into hybrid photovoltaic–chemical systems due to their exceptional optoelectronic properties and low fabrication costs. (Jeon *et al*., 2018). Numerical simulation tools based on drift–diffusion theory, particularly SCAPS-1D, have been extensively employed to investigate the effects of absorber thickness, defect density, interface properties, and carrier transport mechanisms on perovskite solar-cell performance." (Abdelaziz *et al*., 2021). However, these approaches do not explicitly account for the interaction between charge transport within the device and surface reaction kinetics. Although these simulations provide detailed information on device physics and photovoltaic performance metrics, they generally evaluate charge

transport independently of the chemical processes that consume photogenerated carriers. Consequently, the ability of the photovoltaic device to sustain surface reactions under varying kinetic demands remains insufficiently understood.

Surface reactions in photocatalytic and photoelectrochemical systems are frequently described using kinetic models such as the Langmuir–Hinshelwood formalism, which accounts for adsorption, desorption, and reaction processes occurring at active interfaces." (Langmuir, 1918). These models typically assume a sufficient supply of charge carriers and therefore neglect the limitations imposed by photovoltaic transport processes.

Recent studies in photoelectrochemical systems have highlighted the importance of balancing charge transport and interfacial reaction rates to achieve optimal performance (Vargas *et al*., 2020). However, a quantitative framework directly linking photovoltaic output to reaction kinetics remains limited. Dimensionless analysis has been widely employed in chemical reaction engineering and transport phenomena to identify dominant mechanisms and characterize regime transitions. Parameters such as the Damköhler number provide valuable insight into the competition between transport and reaction processes. However, similar dimensionless frameworks remain largely unexplored for coupled photovoltaic–reaction systems.

Despite extensive advances in photovoltaic device modeling and surface reaction kinetics, a unified framework capable of quantitatively linking electron transport within photovoltaic devices to the kinetic demand of surface reactions remains unavailable. Furthermore, existing studies lack a simple predictive criterion for identifying the operating conditions under which system performance becomes transport-limited or reaction-limi Suggested text:

Accordingly, the objective of this study is to develop a transport–reaction coupling framework that directly links photovoltaic charge transport to surface reaction kinetics through a dimensionless flux–kinetics parameter. Using SCAPS-1D simulations of a SnO_2/$CsPbI_2Br$/CuI perovskite solar cell, electron flux values are extracted and related to reaction-rate constants to identify transitions between reaction-limited and transport-limited operating regimes. In particular, existing models do not provide a direct metric to determine whether system performance is limited by electron supply or reaction kinetics. This gap limits the ability to design and optimize coupled photovoltaic–reaction systems.

The proposed framework establishes a quantitative basis for evaluating the compatibility between photovoltaic charge generation and surface reaction demand. By identifying critical transport–reaction transition conditions, the approach provides a practical tool for the design and optimization of photovoltaic-driven photocatalytic, photoelectrochemical, and solar-fuel-generation systems. Furthermore, the framework offers a generalized dimensionless methodology that can be extended to a wide range of coupled energy-conversion technologies.

2.0 Materials and Methods

2.1 Device Structure and Simulation Framework

The photovoltaic device was modeled using SCAPS-1D, a one-dimensional simulation tool based on the drift–diffusion formalism (Burgelman *et al*., 2000), which self-consistently solves Poisson's equation and carrier continuity equations. The simulated architecture consists of a planar heterojunction structure comprising SnO_2 as the electron transport layer (ETL), $CsPbI_2Br$ as the absorber layer, and CuI as the hole transport layer (HTL). This specific all-inorganic architecture was selected to eliminate volatile organic components (such as MA or FA cations), thereby providing an intrinsically stable photovoltaic core suitable for the harsh chemical and thermal environments typical of coupled catalytic operations.

The choice of materials is motivated by their favorable band alignment and charge transport properties, which enable efficient carrier extraction and reduced recombination losses in inorganic perovskite solar cells. The physical, optical, and electronic parameters compiled in Table 1 are extracted from validated experimental literature and standard benchmarking studies to ensure that the baseline simulation closely replicates realistic device behavior

Table 1. SCAPS Input Parameters Used in Simulation

Parameter	SnO_2 (ETL)	$CsPbI_2Br$ (Absorber)	CuI (HTL)
Thickness (µm)	0.2	0.5	0.2
Bandgap, Eg (eV)	3.6	1.88	2.98
Electron Affinity, χ (eV)	4.0	3.82	2.1
Dielectric Permittivity	9.0	8.5	6.5
Nc (cm^{-3})	2.2×10^{18}	2.0×10^{18}	2.8×10^{19}
Nv (cm^{-3})	1.8×10^{19}	2.0×10^{18}	1.0×10^{19}
Electron Mobility, µn (cm^2/Vs)	100	20	1
Hole Mobility, µp (cm^2/Vs)	10	20	20
Donor Density, ND (cm^{-3})	1.0×10^{18}	0	0
Acceptor Density, NA (cm^{-3})	0	0	1.0×10^{17}
Bulk Defect Density, Nt (cm^{-3})	1.0×10^{15}	5.0×10^{14}	1.0×10^{14}

2.2 Interface and Contact Modeling

To accurately capture recombination processes at heterojunction interfaces, defect states were introduced at both the ETL/absorber and absorber/HTL interfaces. These defects were modeled as single-level traps within the bandgap, with parameters summarized in Table 2.

2.2 Simulation Conditions and Thickness Variation

All simulations were performed under standard AM1.5G illumination at an operating temperature of 300 K. Optical absorption within the multilayer stack was modeled using the internal absorption coefficients (α) of the respective materials, assuming an ideal flat-surface reflection profile to isolate the pure bulk transport-reaction phenomena from external geometric texturing effects.

Ohmic contacts were assumed at both electrodes, with work functions chosen to ensure efficient carrier extraction and minimal contact resistance. The contact parameters are provided in Table 3.

To investigate the influence of absorber thickness on device performance, the thickness of the $CsPbI_2Br$ layer was systematically varied from 0.2 µm to 1.2 µm, while keeping all other parameters constant. For each thickness, the current–voltage (I–V) characteristics were computed, and the maximum power point current density (J_{mpp}) was extracted.

Table 2. Interface Defect Parameters

Interface	Defect Density (cm^{-2})	Energy Level (eV)
SnO_2 / $CsPbI_2Br$	1.0×10^{10}	0.6
$CsPbI_2Br$ / CuI	1.0×10^{10}	0.6

Table 3. Contact Parameters

Contact	Work Function (eV)
Front Contact	5.2
Back Contact	4.4

This approach enables isolation of thickness-dependent effects, including optical absorption enhancement and recombination-induced limitations.

2.2 Charge Transport Model

Carrier transport within the device is described using the one-dimensional drift–

diffusion formalism, which is solved self-consistently with Poisson's equation to determine the electrostatic potential and carrier distributions throughout the multilayer structure (Sze & Ng, 2007).

2.3 Governing Equations

2.3.1 Poisson's Equation

$$\frac{d}{dx}\left(\varepsilon\frac{d\psi}{dx}\right) = -q(p - n + N_D^+ - N_A^-) \quad (1)$$

Where (ε) = dielectric permittivity F·cm^{-1}), (ψ) = electrostatic potential (V), (q) = lementary charge (1.602 × 10^{-19} C), (n, p) = electron and hole densities (cm^{-3}), (N_D^+, N_A^-) = ionized donor and acceptor densities (cm^{-3}).

This equation governs the spatial distribution of the electric field inside the device.

The electric field is defined as

$$E = -\frac{d\psi}{dx} \quad (1)$$

2.3.2 Electron and Hole Current Density Equations

$$J_n = q\mu_n nE + qD_n\frac{dn}{dx} \quad (2)$$

$$J_p = q\mu_p pE - qD_p\frac{dp}{dx} \quad (3)$$

Where (J_n, J_p) = current densities (A·cm^{-2}), (μ_n, μ_p) = carrier mobilities (cm^2·V^{-1}·s^{-1}), (D_n, D_p) = diffusion coefficients (cm^2·s^{-1}).

The diffusion coefficients satisfy the Einstein relation:

$$D_{n,p} = \mu_{n,p}\frac{k_B T}{q} \quad (4)$$

with

(k_B) = Boltzmann constant (8.617 × 10^{-5} eV·K^{-1}), (T) = temperature (K).

2.3.3 Carrier Continuity Equations

$$\frac{dJ_n}{dx} = q(G - R) \quad (5)$$

$$\frac{dJ_p}{dx} = -q(G - R) \quad (6)$$

Were

(G) = generation rate (cm^{-3}·s^{-1}), (R) = recombination rate (cm^{-3}·s^{-1}).

These equations enforce local balance between generation, recombination, and transport.

2.3.4 Recombination Model

Because metal halide perovskites are highly sensitive to processing conditions, performance bottlenecks are heavily dictated by deep-level traps. Therefore, non-radiative recombination pathways are explicitly governed by the steady-state Shockley–Read–Hall (SRH) expressionTrap-assisted recombination is modeled using the Shockley–Read–Hall (SRH) expression:

$$R = \frac{np - n_i^2}{\tau_p(n + n_1) + \tau_n(p + p_1)} \quad (7)$$

where

(n_i) = intrinsic carrier density (cm^{-3}), (τ_n, τ_p) = carrier lifetimes (s).

Auxiliary terms:

$$n_1 = n_i exp!\left(\frac{E_t - E_i}{k_B T}\right), \quad p_1 = n_i exp!\left(\frac{E_i - E_t}{k_B T}\right) \quad (8)$$

Equation 9 is satisfied with (E_t) = trap energy level (eV) and (E_i) = intrinsic Fermi level (eV).

This formulation captures recombination via bulk and interface defect states.

2.4 Boundary Conditions

The implementation of these Dirichlet and boundary recombination conditions ensures a physically realistic carrier collection profile, preventing unphysical charge accumulation at the extraction contacts during the thickness sweep.

2.4.1 Electrical Contacts (Ohmic)

At (x = 0) (front) and (x = L) (back):

$$\psi = \psi_{contact} \quad (9)$$

Carrier densities follow equilibrium with contact work functions, ensuring:

$$n = n_0, \quad p = p_0 \quad (10)$$

where equilibrium carrier densities are determined by the contact work functions.

This corresponds to Dirichlet boundary conditions, ensuring efficient carrier extraction and negligible contact resistance.

2.4.2 Interface Recombination

At ETL/absorber and absorber/HTL interfaces:

$$J_n = qS_n(n - n_{eq}),\ J_p = qS_p(p - p_{eq}) \quad (11)$$

Where

(S_n, S_p) = interface recombination velocities (cm·s^{-1}), (n_{eq}, p_{eq}) = equilibrium carrier densities.

2.4.3 Continuity Conditions

At each interface:

$$\psi_1 = \psi_2, \quad J_{n1} = J_{n2}, \quad J_{p1} = J_{p2} \quad (12)$$

ensuring conservation of current across material boundaries.

2.5 Electron Flux and Transport–Reaction Coupling

2.5.1 Electron Flux Definition

The electron flux delivered to the interface is obtained from:

$$\Phi_e = \frac{J_{MPP}}{q} \quad (13)$$

where (Φ_e) = electron flux ($cm^{-2} \cdot s^{-1}$), (J_{MPP}) = current density at maximum power point ($A \cdot cm^{-2}$).

This represents the maximum rate of electron supply available for interfacial reactions.

2.5.2 Physical Interpretation

The coupled solution of Poisson's equation and the continuity equations enables accurate determination of:

- Internal electric field distribution
- Carrier transport dynamics
- Recombination losses

In the present study, thickness-dependent variations in device performance are primarily governed by the competition between carrier generation and SRH recombination, which directly impacts the extractable current density and electron flux.

As the absorber thickness increases:

- $G \uparrow$ due to enhanced optical absorption
- $R_{SRH} \uparrow$ due to increased carrier residence time

This leads to flux saturation, which ultimately limits the transport–reaction coupling.

Recombination processes were modeled using the Shockley–Read–Hall (SRH) formalism, incorporating both bulk and interface defect states as defined in Tables 1 and 2.

2.5.3 Dimensionless Transport–Reaction Parameter

To quantify the interplay between transport and surface kinetics, a dimensionless parameter is introduced:

$$\Phi = \frac{\Phi_e}{k} \quad (14)$$

were, (k) — effective surface reaction rate constant ($cm^{-2} \cdot s^{-1}$)

2.5.3 Physical Interpretation (Damköhler Analogy)

Crucially, the dimensionless parameter Φ functions as an exact photovoltaic analog to the traditional chemical engineering Damköhler number (D_a), mapping the competitive operational timescales of internal electronic transport against external interfacial catalytic conversion

The parameter (Φ) is analogous to a Damköhler number, representing the ratio of:

- Transport supply (Φ_e)
- Reaction demand (k)

Therefore,

- $\Phi \gg 1$: Reaction-limited regime
- $\Phi \approx 1$: Balanced regime
- $\Phi \ll 1$: Transport-limited regime

2.5.4 Thickness Dependence

The transport chain governing this coupling is:

$$G(x); \rightarrow; n(x), p(x); \rightarrow; J(x); \rightarrow; J_{mpp}; \rightarrow; \Phi_e$$

As absorber thickness increases:

- $(G \uparrow)$ (enhanced absorption), $(R \uparrow)$ (increased recombination)

leading to flux saturation, which limits further increase in (Φ).

Similar coupling approaches between transport and reaction processes have been discussed in electrochemical and photocatalytic systems (Vargas *et al*., 2020) By mapping this dimensionless ratio across a wide phase space of absorber dimensions and kinetic constants, the framework systematically identifies the exact threshold where structural modifications yield diminishing returns.

2.5.4 Simulation Workflow and Reproducibility

The simulation procedure follows:

1. Define material parameters (Table 1)
2. Implement interface defect states (Table 2)
3. Apply boundary conditions (Table 3)
4. Perform thickness sweep (0.2–1.2 μm)
5. Extract:
   - (J_{mpp})

6. Compute:
   - $(\Phi_e = J_{mpp}/q)$
   - $(\Phi = \Phi_e/k)$

All simulations are performed under identical numerical conditions to ensure consistency and reproducibility. Finally, the extractable electron flux (Φ_e) is mathematically coupled to a dynamic continuum of surface reaction rate constants ($k = 10^{14\text{ to }}10^{19}\ \text{cm}^{-2}\cdot\text{s}^{-1}$), constructing a multi-dimensional regime map that delineates system limitations under varying operational constraints

3.0 Results and Discussion

3.1 Photovoltaic Device Performance

Fig. 1 shows the dependence of the maximum power point current density (J_{mpp}) on absorber thickness, revealing a clear non-linear trend. As the thickness increases from 0.2 µm to 1.2 µm, J_{mpp} rises from approximately 9.8 to 15.6 mA·cm^{-2}, with a steep increase at low thickness (0.2–0.5 µm) followed by gradual saturation at higher values.

This behavior reflects the competing roles of optical absorption and recombination. At small thicknesses, limited photon absorption restricts carrier generation, resulting in lower current output. Increasing thickness enhances light absorption and carrier generation, leading to a rapid improvement in J_{mpp}. However, beyond ~0.6–0.8 µm, the benefit diminishes as recombination losses become more pronounced, offsetting further gains in absorption.

The observed saturation indicates the presence of an optimal thickness window where generation and recombination are balanced. Importantly, this trend sets an upper limit on the extractable electron flux, which directly governs the transport–reaction coupling analyzed in subsequent sections. The saturation observed beyond 0.8 µm agrees with the findings of Eperon et al. (2014), who reported that increased absorber thickness improves light harvesting only until recombination losses begin to dominate. The present results extend this understanding by demonstrating that such saturation also imposes a limit on transport-driven surface reaction rates.

(Eperon *et al*., 2014).

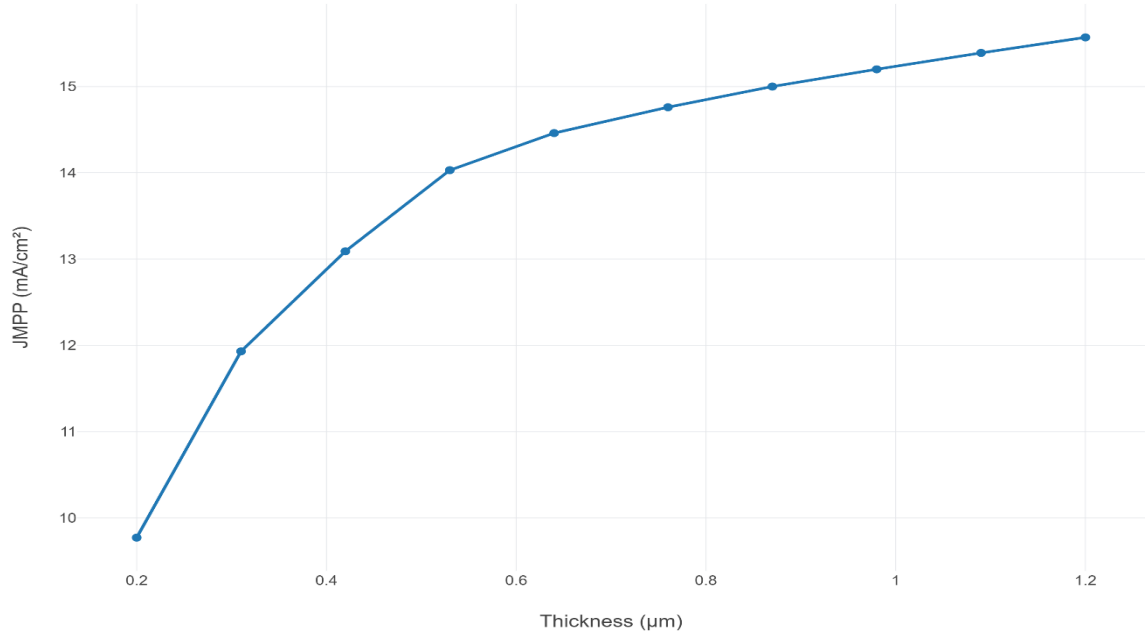

Fig. 1. Variation of maximum power point current density (J_{mpp}) as a function of absorber thickness (0.2–1.2 µm) for the SnO_2/$CsPbI_2Br$/CuI perovskite solar cell. The current density increases rapidly at low thickness due to enhanced photon absorption, followed by saturation at higher thicknesses as recombination losses become dominant.

3.2 Electron Flux Analysis

Fig. 2 shows the variation of electron flux (Φ_e) with absorber thickness, exhibiting a non-linear increase from $\sim 6.1 \times 10^{16}$ *to* $9.7 \times 10^{16}\ cm^{-2}.s^{-1}$ as thickness increases from 0.2 µm to 1.2 µm. The rise is steep at low thicknesses but gradually saturates beyond ~0.6–0.8 µm.

This trend closely follows that of J_{mpp}, reflecting their direct proportionality. At small thicknesses, limited absorption constrains carrier generation and reduces electron supply. Increasing thickness enhances photogeneration and thus electron flux. However, once most incident photons are absorbed, further thickness primarily increases recombination, leading to a diminishing gain in Φ_e.

The resulting flux saturation highlights a fundamental transport limitation: beyond an optimal thickness, the device cannot significantly increase the electron supply available for interfacial processes. This directly constrains the maximum achievable reaction rate and underpins the transition between transport-limited and reaction-limited regimes discussed later. Similar saturation behavior has been reported in SCAPS-based studies of perovskite solar cells (Hima *et al*., 2021).

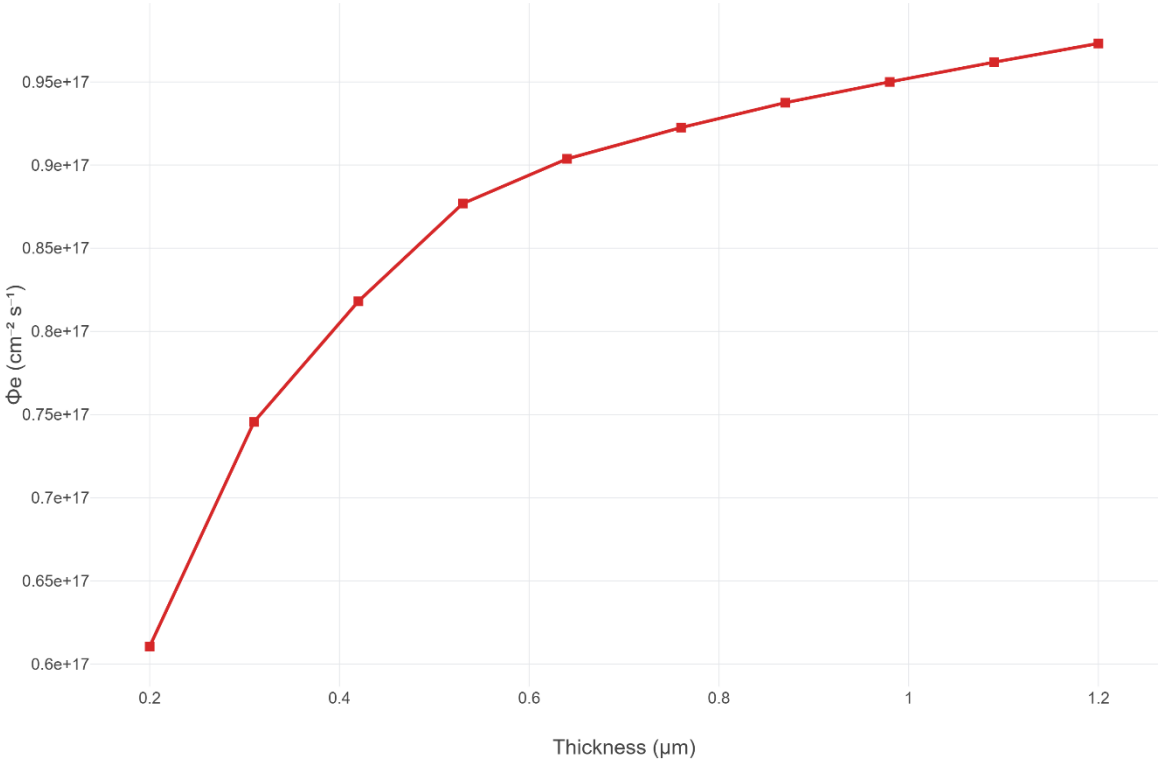

Fig. 2. Electron flux (Φ_e) derived from the maximum power point current density as a function of absorber thickness. The flux exhibits a non-linear increase with thickness and approaches saturation at higher values, reflecting the balance between carrier generation and recombination processes

3.3 Coupled Transport–Reaction Behavior

Fig. 3 illustrates the variation of the coupling parameter (Φ) with reaction rate constant (k) for different absorber thicknesses. On a log–log scale, Φ decreases linearly with k, exhibiting a slope of approximately −1, consistent with the relation $\Phi = \Phi_e/k$. This confirms that the coupling behavior follows a well-defined inverse scaling.

Three operating regimes are clearly distinguished. At low reaction rates ($k \leq 10^{14}$), $\Phi \gg 1$, indicating a reaction-limited

regime where electron supply exceeds demand. At high reaction rates ($k \geq 10^{17}$), $\Phi \ll 1$, and the system becomes transport-limited due to insufficient electron flux. The transition occurs at $\Phi = 1$, where transport and reaction are balanced.

"To the best of our knowledge, this provides the first SCAPS-derived dimensionless criterion for identifying the transition between photovoltaic transport limitation and reaction limitation in coupled photovoltaic-reaction systems.

Increasing absorber thickness shifts this transition toward higher k, indicating that thicker devices can sustain faster reactions. However, this shift becomes progressively smaller at larger thicknesses, reflecting the saturation of electron flux.

Overall, these results show that while thickness influences the transport–reaction balance, its impact is fundamentally constrained. The saturation of Φ_e imposes a limit beyond which further thickness increases do not significantly extend the operational range, highlighting the need for simultaneous optimization of both device transport properties and reaction kinetics.

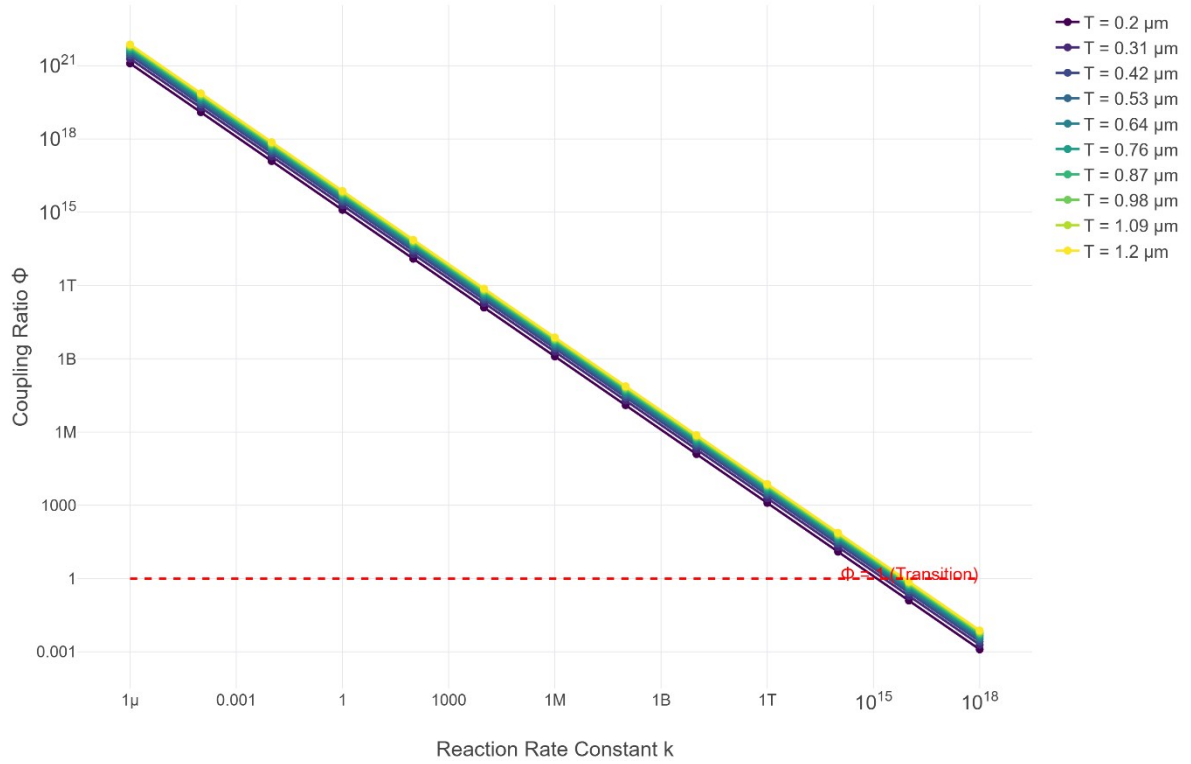

Fig. 3. Coupling ratio ($\Phi = \Phi_e/k$) as a function of reaction rate constant (k) for different absorber thicknesses. The linear decrease of Φ on a log–log scale indicates an inverse relationship with k. The horizontal dashed line ($\Phi = 1$) denotes the transition between reaction-limited ($\Phi \gg 1$) and transport-limited ($\Phi \ll 1$) regimes.

3.4 Regime Mapping of Transport and Reaction Limitations

Fig. 4 presents a two-dimensional regime map of the coupling parameter (Φ) as a function of absorber thickness and reaction rate constant, with the color scale representing $\log_{10}(\Phi)$. The map clearly delineates the transition between reaction-limited ($\Phi \gg 1$) and transport-limited ($\Phi \ll 1$) regimes.

A key feature is the presence of nearly vertical transition boundaries, indicating that system behavior is governed predominantly by the reaction rate constant rather than absorber thickness. At low reaction rates, the system remains reaction-limited across all thicknesses, whereas at high reaction rates, it

becomes transport-limited due to insufficient electron flux. Although increasing thickness slightly shifts the transition toward higher reaction rates, this effect is weak and progressively diminishes. This limited sensitivity arises from the saturation of electron flux, which constrains the extent to which thickness can enhance charge supply.

Overall, the regime map demonstrates that reaction kinetics is the primary control parameter, while thickness plays a secondary role. This highlights a critical design implication: optimizing absorber thickness alone is insufficient to expand the operational window, and effective performance requires coordinated tuning of both transport properties and reaction kineticsBecause the variation in electron flux across the investigated thickness range is less than one order of magnitude, whereas the reaction rate constant spans several orders of magnitude, the reaction kinetics exerts a stronger influence on the coupling parameter than absorber thickness.

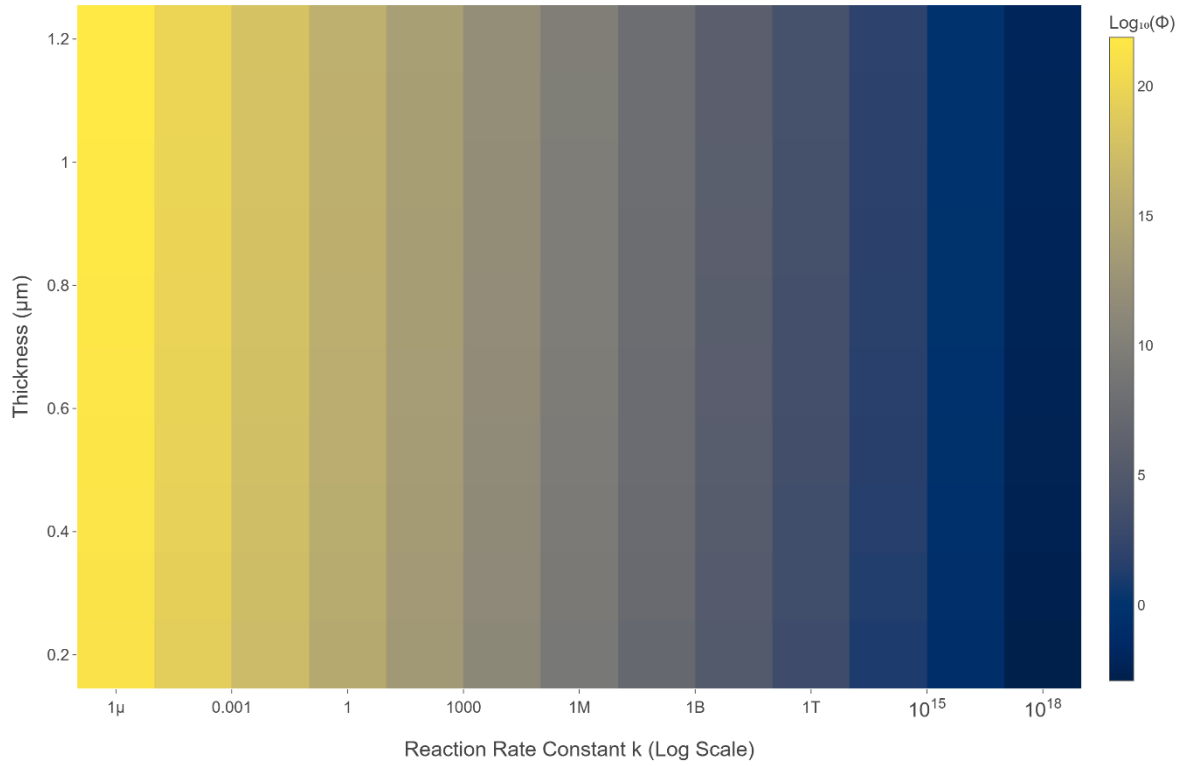

Fig. 4. Regime map of the coupling ratio ($\log_{10}\Phi$) as a function of absorber thickness and reaction rate constant. The color scale distinguishes reaction-limited and transport-limited regions. The nearly vertical transition boundary highlights the dominant influence of reaction kinetics over thickness

3.5 Thickness-Dependent Transition Boundary

Fig. 5 shows the dependence of the critical reaction rate constant ($k_{critical}$, defined at Φ=1) on absorber thickness. As thickness increases from 0.2 μm to 1.2 μm, $k_{critical}$ rises from approximately $1.1.2 \times 10^{15}$ to 7.5×10^{15}, with a rapid increase at low thickness followed by clear saturation at higher values.

This trend directly reflects the relationship $k_{critical} = \Phi_e$. At small thicknesses, limited absorption restricts carrier generation and electron flux, resulting in a low kcriticalk_{critical}kcritical and an early onset of transport limitation. Increasing thickness enhances flux and allows the system to sustain higher reaction rates. However, as recombination becomes

dominant, the flux—and thus $k_{critical}$—approaches a maximum value.

The observed saturation reveals a fundamental constraint: beyond an optimal thickness, further geometric scaling does not significantly extend the achievable reaction rate. This underscores that absorber thickness alone cannot overcome intrinsic transport limits, and that effective system optimization requires simultaneous control of both charge transport and reaction kinetics. Similar transport–reaction transitions have been reported in photoelectrochemical and catalytic systems (Vargas *et al*., 2020).

It should be noted that the present framework is based on one-dimensional SCAPS simulations and assumes idealized reaction kinetics represented by a single rate constant. In practical photovoltaic-reaction systems, additional factors such as interfacial charge-transfer resistance, catalyst morphology, surface states, and mass-transfer effects may influence the transport-reaction balance. Nevertheless, the proposed dimensionless approach provides a useful first-order framework for identifying dominant operating regimes and guiding system optimization.

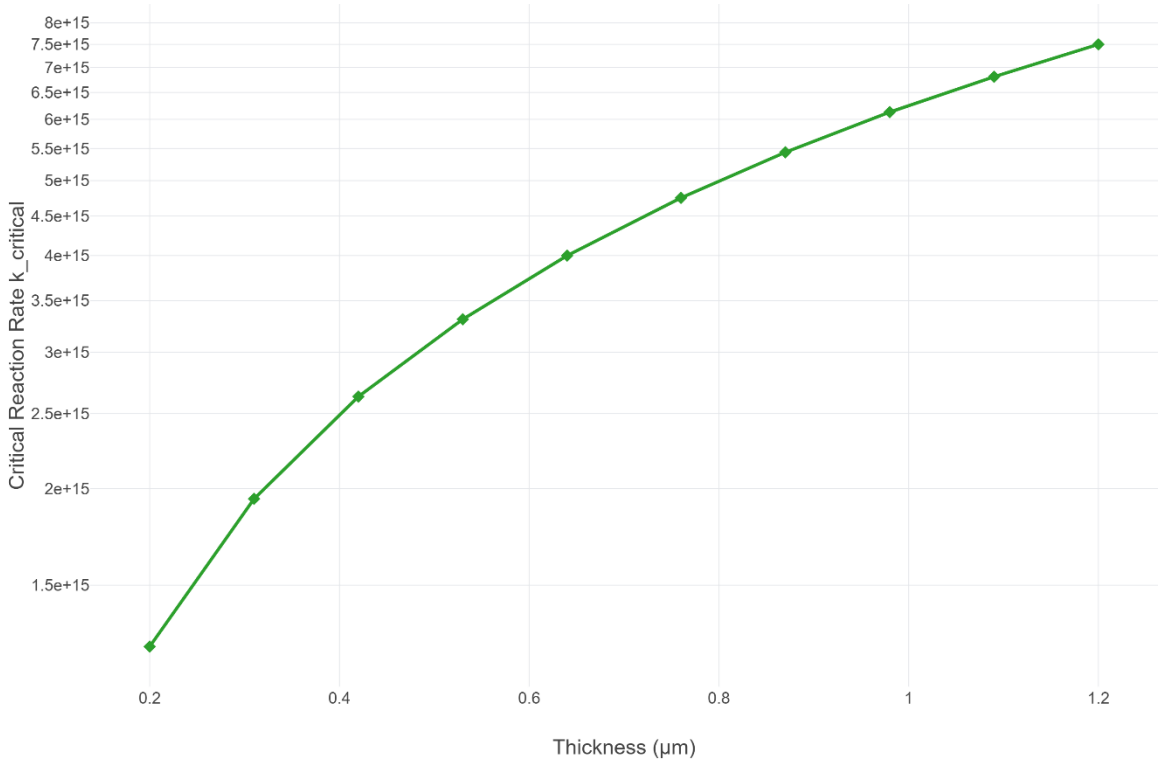

Fig. 5. Critical reaction rate constant (k_{critical}) as a function of absorber thickness, defined at the transition condition $\Phi = 1$. The non-linear increase followed by saturation indicates that the maximum sustainable reaction rate is limited by the saturation of electron flux at higher thickness values.

Overall, the results demonstrate that absorber thickness influences photovoltaic performance, electron flux, and transport-reaction coupling primarily through its effect on charge generation and recombination. The introduction of the dimensionless coupling parameter Φ reveals a clear transition between reaction-limited and transport-limited regimes, with the critical boundary occurring at Φ = 1. Although increasing thickness enhances electron supply, the associated flux eventually saturates, limiting the maximum sustainable reaction rate. These findings establish a quantitative framework for evaluating and optimizing coupled photovoltaic-reaction systems and highlight

the necessity of jointly tailoring charge transport properties and reaction kinetics to achieve maximum performance.

4.0 Conclusion

This study developed a dimensionless transport–reaction framework that directly links photovoltaic charge transport with surface reaction kinetics in coupled photovoltaic–reaction systems. Using SCAPS-1D simulations of a SnO_2/$CsPbI_2Br$/CuI perovskite solar cell, the analysis revealed that electron flux increases with absorber thickness but eventually saturates due to recombination losses, rising from approximately 6.1×10^{16} to 9.7×10^{16} $cm^{-2}\ s^{-1}$ over the investigated thickness range. The results further demonstrated a clear transition between reaction-limited ($\Phi \gg 1$) and transport-limited ($\Phi \ll 1$) regimes, with the critical boundary occurring at $\Phi = 1$ and corresponding reaction rates on the order of 10^{16}–10^{17} s^{-1}.

The findings show that absorber thickness can enhance charge supply only up to a saturation limit, beyond which further increases provide diminishing benefits. Consequently, the operational performance of coupled photovoltaic–reaction systems is governed primarily by the balance between transport supply and reaction demand rather than by photovoltaic efficiency alone. The proposed framework provides a simple and generalizable tool for identifying performance bottlenecks and guiding the co-optimization of charge transport and reaction kinetics in photovoltaic-driven photocatalytic, photoelectrochemical, and solar-fuel-generation technologies. Future studies should focus on experimental validation and extension of the framework to more complex reaction networks and multidimensional transport models.

5.0 References

Abdelaziz, S., Zekry, A., Shaker, A., & Abouelatta, M. (2021). Numerical simulation of perovskite solar cells using SCAPS-1D: A comparative study. *Optik*, *223*, Article 165641.

Burgelman, M., Nollet, P., & Degrave, S. (2000). Modelling polycrystalline semiconductor solar cells. *Thin Solid Films*, *361*, 527–532.

Eperon, G. E., Burlakov, V. M., Docampo, P., Goriely, A., & Snaith, H. J. (2014). Morphological control for high performance, solution-processed planar heterojunction perovskite solar cells. *Advanced Functional Materials*, *24*, 151–157.

Fujishima, A., & Honda, K. (1972). Electrochemical photolysis of water at a semiconductor electrode. *Nature*, *238*(5358), 37–38. https://doi.org/10.1038/238037a0

Gong, J., Li, C., & Wasielewski, M. R. (2019). Advances in solar energy conversion. *Chemical Society Reviews*, *48*, 1862–1864.

Hima, A., Lakhdar, M., Benghanem, S., & Saadoune, A. (2021). Simulation of high efficiency perovskite solar cells using SCAPS-1D. *Materials Today: Proceedings*, *45*, 7463–7467.

Jeon, N. J., Na, H., Jung, E. H., Yang, T. Y., Lee, Y. G., Kim, G., Shin, H. W., Seok, S. I., Lee, J., & Seo, J. (2018). A fluorene-terminated hole-transporting material for highly efficient and stable perovskite solar cells. *Nature Energy*, *3*, 682–689.

Langmuir, I. (1918). The adsorption of gases on plane surfaces of glass, mica and platinum. *Journal of the American Chemical Society*, *40*, 1361–1403.

Sze, S. M., & Ng, K. K. (2007). *Physics of semiconductor devices* (3rd ed.). Wiley.

Vargas, R., Carvajal, D., Madriz, L., & Scharifker, B. R. (2020). Chemical kinetics in solar to chemical energy conversion. *Energy Reports*, *6*, 315–325.

Declarations

Consent for Publication

All authors have read and approved the final version of the manuscript and consent to its publication.

Funding

This research received no specific grant from any funding agency in the public, commercial, or not-for-profit sectors.

Ethical Approval and Consent to Participate

Not applicable. This study is based entirely on numerical simulation and computational modeling using the SCAPS-1D software and did not involve human participants, animals, or biological materials.

Availability of Data and Materials

All data generated or analyzed during this study are included in this published article. Additional information, simulation parameters, and supporting materials are available from the corresponding author upon reasonable request.

Competing Interests

The authors declare that they have no known competing financial interests or personal relationships that could have appeared to influence the work reported in this paper.

Author Contributions

Ejikeme Ezo Igbokwe conceived the study, developed the theoretical framework, designed the simulation methodology, performed the SCAPS-1D simulations, analyzed and interpreted the data, prepared the figures, and wrote the original manuscript. Ho Soonmin contributed to the conceptual development of the transport–reaction coupling framework, supervised the research, validated the methodology and results, critically reviewed and revised the manuscript for important intellectual content, and approved the final version for publication. Both authors read and approved the final manuscript.

Acknowledgements

The authors sincerely acknowledge the developers of the SCAPS-1D simulation software for providing an invaluable computational platform for photovoltaic device modeling. The authors also appreciate the support of their respective institutions throughout the course of this research.